Amphiphiles formed from synthetic DNA-nanomotifs mimic the dispersal of transcriptional clusters in the cell nucleus

Xenia Tschurikow[1,2], Aaron Gadzekpo[1,2], Mai P. Tran[3,4], Rakesh Chatterjee[5,6], Marcel Sobucki[1], Vasily Zaburdaev[5,6], Kerstin Göpfrich[3,4], and Lennart Hilbert[1,2,*]

[1]Institute of Biological and Chemical Systems, Karlsruhe Institute of Technology
[2]Zoological Institute, Karlsruhe Institute of Technology
[3]Center for Molecular Biology of Heidelberg University (ZMBH)
[4]Max Planck Institute for Medical Research
[5]Max Planck Zentrum für Physik und Medizin
[6]Chair of Mathematics in Life Sciences, Friedrich-Alexander Universität Erlangen-Nürnberg
[*]Corresponding author, e-mail: lennart.hilbert@kit.edu

Abstract

The formation of biomolecular condensates by phase separation can be mimicked using fully synthetic, phase-separating DNA-nanomotifs, enabling remarkable control and performance increase in several functional nanomaterials. Stem cells exhibit prominent clusters of macromolecules controlling and executing transcription of genes into RNA, which also form via a phase-separation mechanism. Genes that become transcribed can unfold or even disperse these clusters due to an amphiphilic effect. Here, we deploy amphiphilic DNA-based nanomotifs with a nanomotif-repellent poly-thymine tail to recreate the biologically observed, inducible dispersal for droplets formed from DNA-nanomotifs. We use super-resolution microscopy images of transcriptional clusters in pluripotent zebrafish embryo cells as biological reference data. Time-lapse microscopy, amphiphile titration experiments, and Langevin dynamics simulations demonstrate that the addition of amphiphile-motifs to the synthetic system reproduces the shape changes and dispersal seen for transcriptional clusters in the embryonic cells. Our work illustrates how organization principles of biological model systems can guide the implementation of novel ways to control the mesoscopic organization of synthetic nanomaterials.

Introduction

Cells need to compartmentalize their molecular components to ensure proper function. Conventionally, such compartmentalization was attributed to cellular organelles that are enclosed by membranes. More recently, processes based on liquid-liquid phase separation (LLPS) on the basis of transient interactions were implicated in sub-cellular compartmentalization [1–3]. Here, theoretical concepts from polymer systems are applied to explain selective and dynamic compartmentalization of specific

molecular components and functions of biological cells. While much debate remains on LLPS in biological cells [3], the transfer of biologically inspired compartmentalization via LLPS into biomimetic and synthetic systems yields remarkable design possibilities and performance increases [4]. A flexible platform for fully programmable, multi-species phase separation is now available via DNA-nanomotifs, whose interactions are based on homologoy of "sticky ends" of exposed, self-complementary single-stranded DNA [5, 6]. This platform has enabled, for example, the construction of a synthetic DNA segregation module that mimics chromosome separation during mitosis [7]. Embedding into DNA-nanomotif droplets has also allowed the combinatorial detection of tumor biomarkers [8]. Further, an up to 20-fold acceleration of DNA-computing operations has been achieved by embedding of DNA-based logic gates within phase-separated droplets [9].

Droplets formed by canonical LLPS coarsen into increasingly larger droplets over time, whereas intra-cellular condensates are typically size-controlled, or, in a state of microphase separation [3, 10, 11]. Size-limited droplets can be established and maintained by different physical mechanisms, including active reaction processes [12, 13], targeted removal of aged droplets [14], or by provision of pinning centers at which droplets are localized [15, 16]. Most commonly, however, microphase separation is attained by the addition of amphiphilic particles characterized by a dual affinity for two separating particle species [17]. For example, engineered amphiphilic proteins with an affinity for a condensate-forming phase and the surrounding dilute phase limit the size of droplets formed from arginine/glyine-rich disorded domains [18]. A similar reduction in droplet size was seen upon the heat stress-induced localization of superoxide dismutase 1 (SOD1) to the surface of stress granules [19]. The amphiphilic protein Ki-67 was found to be required during mitosis to ensure proper segregation of chromosomes and reestablishment of nuclei after cell division [20]. In particular, the C-terminal leucine-arginine domain binds to chromosomes whereas the N-terminal domain shows high affinity to the cytoplasm. When visualizing the eukaryotic genome by microscopy during interphase, a characteristic micro-domain pattern can be seen: DNA-enriched regions with typical diameters of a few 100 nm are scattered throughout a nuclear space that is otherwise depleted of DNA and enriched with RNA [21–25]. A corresponding microdomain pattern was found in euchromatic regions of the genome in mouse and zebrafish stem cells [26]. This pattern is stabilized by sites of ongoing transcription that connect DNA-rich and RNA-rich microdomains. The inhibition of RNA polymerase II (Pol II), the enzyme complex responsible for transcribing most eukaryotic genes, leads to a coarsening of the microdomains into larger domains, as expected for the removal of a stabilizing amphiphile. An amphiphilic effect of ongoing transcription can also be seen by super-resolution microscopy of clusters of transcriptional machinery in stem cells [27]. These clusters form by a phase-separation mechanism [28–35] and unfold or even split into smaller clusters when they are engaged by genes that undergo transcriptional activation [27, 36]. This effect can be reproduced in detail by a polymer model, in which genes are described as amphiphiles that associate with transcriptional clusters formed by liquid condensation [27].

Taken together, these different biological examples all seem to follow the same basic concept: a phase-separating component is combined with an according amphiphile species, leading to droplet size limitation, or, in more extreme cases, complete dispersal of droplets. Here, we extend the synthetic DNA-nanomotif droplet platform by amphiphile-motifs and show that the effect of these amphiphile-motifs closely resembles the dispersal of embryonic transcriptional clusters. To this end, we initially characterize the dispersal of transcriptional clusters in pluripotent zebrafish embryos by instant-SIM super-resolution microscopy. We then synthetically reimplement the theorized phase separation and dispersal processes using nanomotifs formed purely from synthetic DNA oligomers. In addition to the previously developed droplet-forming DNA-nanomotifs with sequence-encoded self-interactions [5], we construct amphiphilic particles, to which a negatively charged, single-stranded poly-thymine (poly-T) tail is added. High-resolution and time-lapse microscopy confirm the expected droplet-surface localization and dispersing effect of the amphiphilic particles. Amphiphile titration experiments and analyses of changes in droplet shape distributions indicate close agreement with the effect of increasing transcription levels in embryonic cells. The general applicability of our results is further supported by a Langevin dynamics simulation containing self-interacting and amphiphilic particles, which reproduce the observations from embryonic cells as well as fully synthetic DNA droplets. Taken together, our

study illustrates how a biophysical principle observed in a biological system can be clarified in numerical simulations and exploited to design and control biomimetic nanomaterials.

Results

Dispersal of RNA polymerase II clusters by an amphiphilic effect of transcribed genes

To allow the comparison of the effect of DNA-based amphiphiles against a biological model system, we first characterize how transcriptional clusters are affected by the amphiphilic effects exerted by transcribed genes. Especially long-lived and pronounced transcriptional clusters can be found in stem cells [28] and during the early development of zebrafish embryos [27]. In the zebrafish embryo, for a number of genes, transient visits to transcriptional clusters occur, which are tightly coupled with the transcriptional control of these genes by so-called "super-enhancers" [36]. As genes engage with transcriptional clusters and transcript elongation begins, transcriptional clusters are dispersed, leading to unfolding or even complete dissolution of clusters (Figure 1A). This effect has been attributed to an amphiphilic property of genes that undergo activation in association with these prominent transcriptional clusters: while these genes exhibit an increased tendency to associate with transcriptional clusters, the beginning of transcript elongation additionally drives the exclusion of these genes from the transcriptional cluster [36].

To obtain a fine-grained assessment of how increasing transcription levels relate to the dispersal of transcriptional clusters in zebrafish embryos, we labeled different regulatory states of Pol II by immunofluorescence. Recruited RNA polymerase II, which serves as a label for transcriptional clusters, can be detected via a specific phosphorylation mark of the RNA polymerase II C-terminal domain (Pol II S5P, Figure 1B). A different phosphorylation mark (Pol II S2P), can be used to detect currently elongating Pol II, which serves as an indicator of ongoing transcript elongation (Figure 1B). Fluorescence images recorded by instant-SIM super-resolution confocal microscopy [37] revealed a range of shapes of the prominent Pol II S5P clusters, exhibiting more unfolding and dispersal for clusters with higher levels of ongoing transcription, as indicated by higher levels of Pol II S2P (Figure 1C). Quantifying the degree of unfolding via the sphericity of the Pol II S5P clusters also substantiates the impression that higher Pol II S2P levels correlate with a less spherical shape of the Pol II S5P clusters (Figure 1C). A comprehensive overview of Pol II S5P cluster shape was obtained via sphericity-volume scatter plots, which revealed that a population of large (volume$\geq 0.08\,\mu\mathrm{m}^3$) and round (sphericity$\geq 0.1$) clusters is present specifically for intermediate levels of elongation activity (Figure 1D). Assessing the fraction of large clusters at a given Pol II S2P level further substantiates the impression that more large clusters occur at intermediate levels of transcript elongation (Figure 1D). When all clusters at a given Pol II S2P level are considered, the median volume of clusters, however, does not change appreciably, indicating that the median volume is dominated by the large fraction of small clusters (Figure 1D). Analyzing therefore the sphericity of only large clusters, an increase at intermediate transcription levels followed by a decrease at high Pol II S2P levels can be detected (Figure 1D). Taken together, these analyses characterize how the amphiphilic effect of transcript elongation correlates with unfolding of clusters, and, at the highest levels of transcript elongation, loss of large clusters.

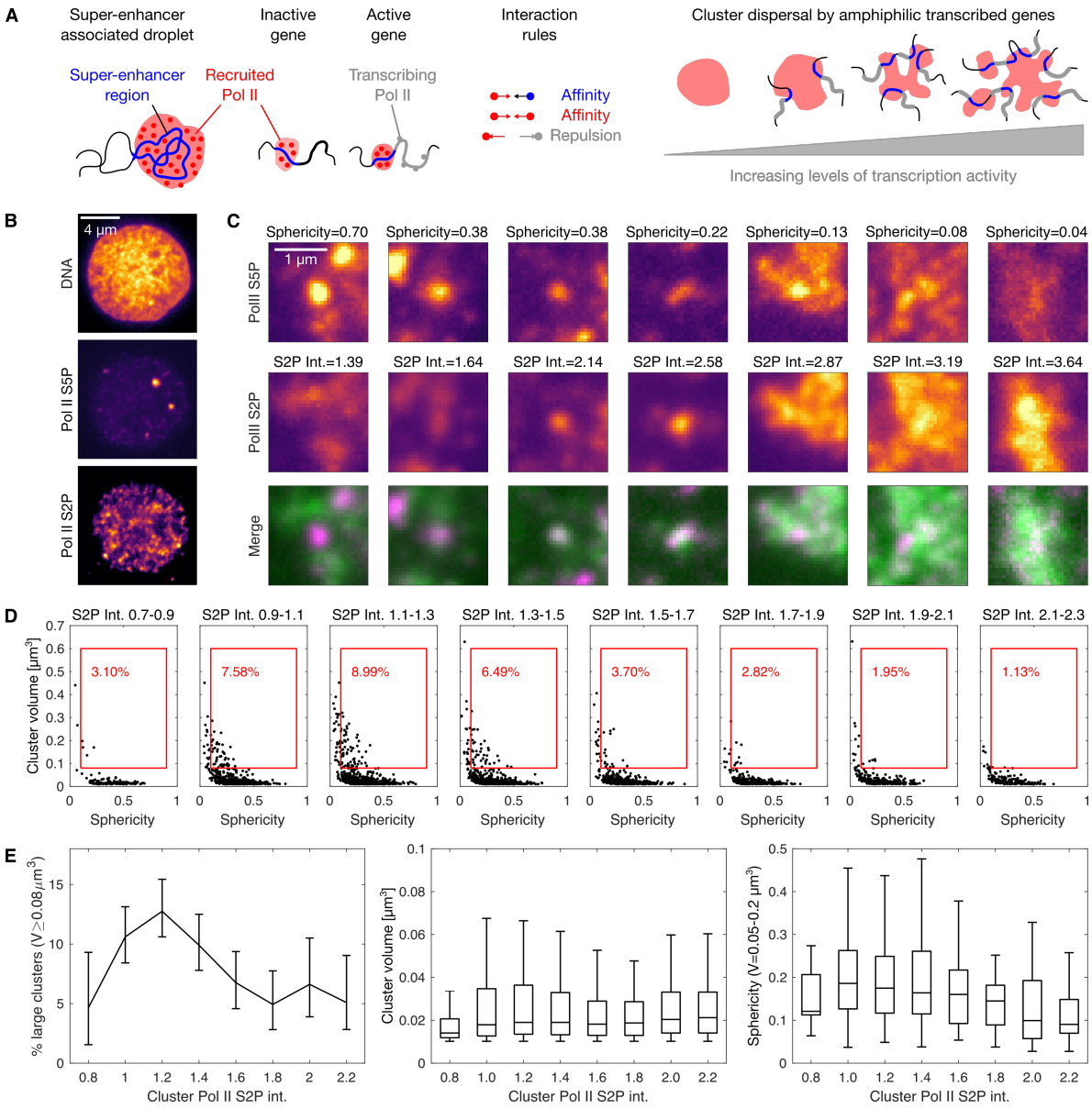

Fig. 1: **Transcribed genes act as amphiphile-like complexes that mediate the dispersal of RNA polymerase II clusters in nuclei of pluripotent zebrafish embryos.** A) Illustration of the formation of clusters of recruited RNA polymerase II at super-enhancer regions of the genome and dispersal of clusters by an amphiphilic effect of transcribed genes. B) Representative three-color micrograph of an optical section through the middle of a cell nucleus in a pluripotent zebrafish embryo (sphere stage of development). Image data obtained by instant-SIM microscopy, color channels show DNA (Hoechst 33342), recruited RNA polymerase II (Pol II S2P, labeled by indirect immunofluorescence), and elongating RNA polymerase II (Pol II S2P, indirect immunofluorescence). C) Detail views of clusters of recruited RNA polymerase II, showing only the Pol II S2P and Pol II S2P channels. Sphericity was obtained from threshold-based segmentation of Pol II S5P clusters, S2P Int. refers to the mean intensity in the Pol II S2P channel, normalized by the median intensity of the nucleus that the cluster is contained in. D) Segmented clusters were binned according to Pol II S2P intensity to generate sphericity-volume distributions. The percentage in red indicates binned clusters with volume $\geq 0.08\,\mu\text{m}^3$ and sphericity ≥ 0.1 (red box). E) Per-bin calculation of the percentage of large clusters in a given bin (volumes of $0.08\,\mu\text{m}^3$ or more, mean with 95% bootstrap confidence interval), volume (all volumes included, box plots of standard quantile ranges), and sphericity (only considering clusters with volume $0.05 - 0.2\,\mu\text{m}^3$ to prevent volume-dependent artefacts). Data obtained from 99 nuclei pooled from 8 embryos.

Design of amphiphile-motifs that can disperse liquid-like droplets formed from self-interacting DNA-nanomotifs

After having characterized the dispersal of transcriptional clusters as a biological reference for the desired amphiphilic effects, we proceeded to develop amphiphiles that disperse droplets formed from DNA-nanomotifs. The phase-separating DNA-nanomotifs, called Y-motifs due their three-ended shape, self-interact via sequence-programmed sticky ends [5]. Corresponding amphiphile-nanomotifs must exhibit an affinity for the droplet-forming Y-motifs as well as a repulsion from high concentrations of these Y-motifs (Figure 2A). While the affinity for Y-motifs can be directly implemented via the sequence-encoded sticky ends, a repulsive effect can be induced, for example, by attaching negative charges to the amphiphile-motif (Figure 2A). The addition of negative charges via 5'-conjugation of a phosphate group as well as via the extension by 102 thymines (poly-T extension) resulted in a visually apparent reduction of droplet diameter, as is expected upon addition of an amphiphile (Figure 2B). Considering that amphiphile-motifs generated via the poly-T extension appeared to result in smaller droplets than the phosphate addition, we used the poly-T-based amphiphile design in the following steps of our study. The apparent dispersal of droplets by these amphiphile-motifs was abolished both when the negatively charged poly-T extension was completely removed or cancelled by the addition of 10 nt-long poly-adenine (poly-A) blocker oligomers (Figure 2C). These results suggest that, indeed, phase-separated droplets formed from self-attracting Y-motifs can be dispersed by amphiphile-motifs in line with the dispersal of transcriptional clusters in the zebrafish embryo.

Amphiphile-motifs localize to droplet surfaces and subsequently disperse droplets

To better understand the dispersal of Y-motif droplets, we added amphiphile-motifs to a suspension containing preformed Y-motif droplets, and visualized both species by time-lapse fluorescence microscopy (Figure 2D). Initially, amphiphile-motifs are homogeneously distributed throughout the volume not occupied by Y-motif droplets and excluded from Y-motif droplets (Figure 2E, 0 min inset). Amphiphile-motifs successively redistribute from outside to within the Y-motif droplets. Upon closer inspection, amphiphile-motifs exhibit a tendency to accumulate more strongly at the surface of Y-motif droplets relative to the inside of the Y-motif droplets, and some of the droplets seem to have undergone splitting into smaller droplets (Figure 2E, 30 min inset). Over time, the redistribution of amphiphile-motifs into the Y-motif droplets becomes yet more pronounced. Also, droplets are surrounded by a more clearly distinguishable layer of amphiphile-motifs and appear generally smaller, as would be expected after further splitting events (Figure 2E, 90 min inset). These observations suggest that amphiphile-motifs are successively redistributed into the Y-motif droplets and become incorporated into droplet surfaces. Over time, large droplets become increasingly energetically unfavourable and split into increasingly smaller droplets.

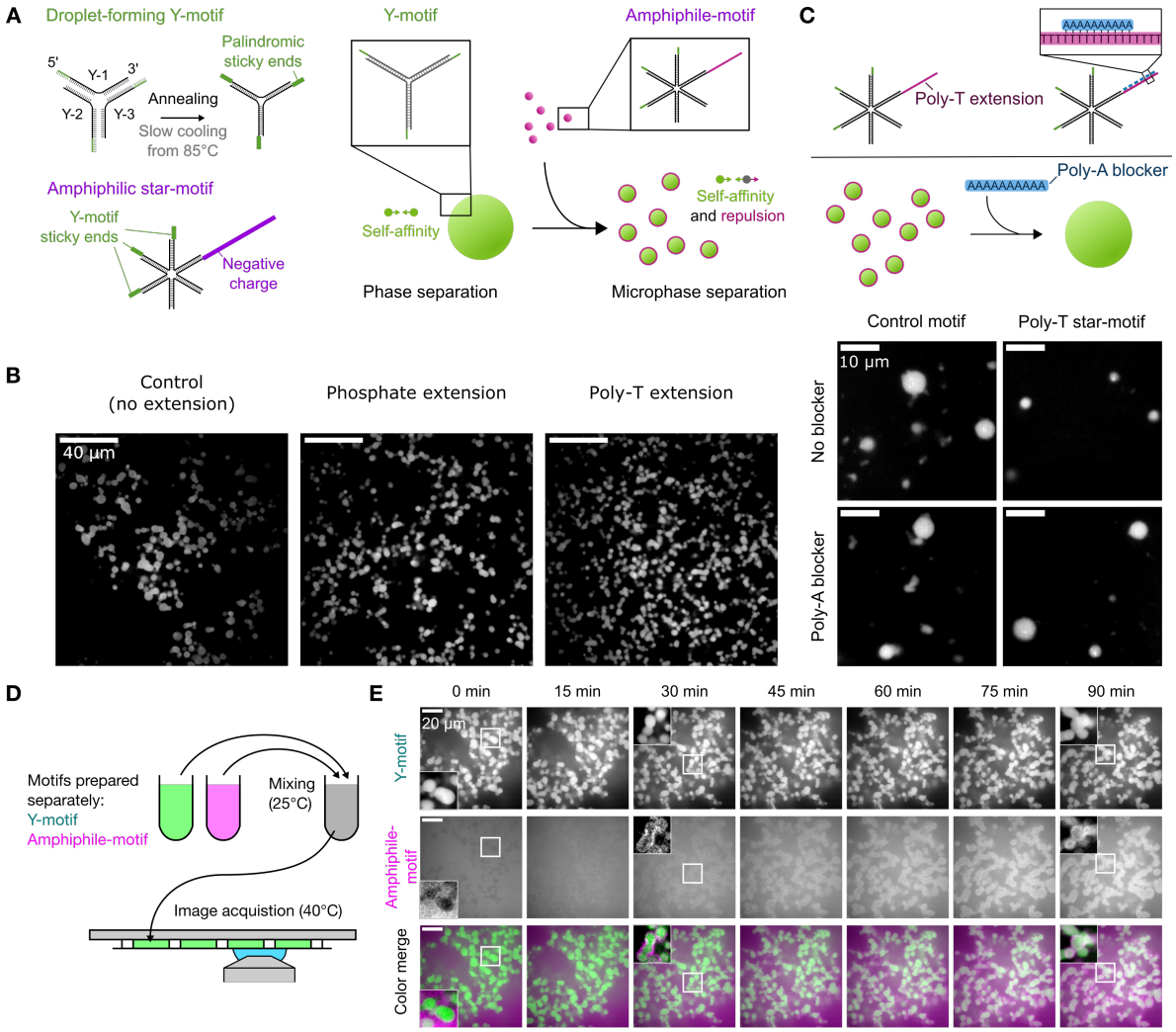

Fig. 2: **Amphiphiles for the dispersal of droplets formed from synthetic DNA-nanomotifs.** A) Illustration of nanomotifs obtained by annealing of single DNA-oligomers, which consist of a 34 nt long core-structure, binding their neighboring strands, and a 8 nt long palindromic sticky end sequence. Amphiphile-motifs are generated by adding negative charge to one vacant end of of a six-ended star motif. Y-motifs form phase-separated droplets due to the self-affinity established by sticky ends, which become dispersed upon the addition of amphiphile-motifs. B) Representative micrographs of Y-motif droplets in the presence of negatively charged star-motifs. The negative charge is added via phosphate conjugation or the extension of one vacant end of the star-motif by 102 thymines (poly-T extension). Images are single confocal sections. C) Illustration of the charge-canceling effect from adding 10 nt long poly-A blockers. Micrographs show single confocal sections of Y-motif droplets in the presence of star-motifs without (control-motif) or with poly-T extension (amphiphile-motif), without or with addition of poly-A blockers. D) Y-motif droplets and amphiphile-motif solution were prepared in separate reaction tubes and subsequently mixed together for time-lapse imaging of the subsequent reorganization processes. E) Representative two-color time-lapse showing single confocal sections obtained from volumetric image stacks originally acquired with a 3-min time interval. Images 3D-deconvolved (Lucy-Richardson), Y-motif channel photo-bleaching (histogram matching method), insets contrast-adjusted to emphasize local details. Results were comparable over three independent repeats with two consecutive time-lapse recordings per repeat.

Shape quantification suggests that droplet dispersal, but not recruitment to droplets is mediated by amphiphilicity

To follow up on the suspected temporal sequence consisting of amphiphile-motif recruitment to Y-motif droplets followed by splitting of Y-motif droplets, we carried out a time-course experiment with precise temperature control (50°C). Y-motif droplets initially took on rounder shapes, became increasingly smaller over time until, ultimately, most droplets vanished (Figure 3A). For the addition of control-motifs, rounding of Y-motif droplets was equally observed. However, instead of becoming smaller, droplets continued to grow over time (Figure 3A). To consolidate these observations by a quantitative analysis, we produced scatter plots of the Y-motif droplet volume and sphericity (Figure 3B). The addition of amphiphile-motifs initially resulted in a shift of the distribution of droplets with high volume from low to high sphericity, reflecting the rounding of droplets. At later time points, the addition of amphiphile-motifs results in the successive loss of droplets at higher volumes, reflecting the visually apparent dispersal of most droplets. The addition of control-motifs, in contrast, results in the occurrence of a persistent population of Y-motif droplets with high volume and sphericity, substantiating the visually apparent emergence of large, round droplets. Guided by the overview obtained from the scatter plots, we more directly confirmed that upon amphiphile addition the number of droplets dropped from 3020 ± 110 to 34.1 ± 2.6 (Figure 3C). The reduction in droplet number is likely caused by the dispersing effect of amphiphile-motifs. For control-motifs, a reduction in droplet number is also observed, most likely resulting from the successive ripening of droplets towards a configuration of fewer and larger droplets. This indicates a divergence in droplet size between addition of the amphiphile- vs. the control-motif. Indeed, the median droplet volume after addition of amphiphile-motif transiently increases from $\approx 0.009\,\mu\text{m}^3$ at 0 min to $\approx 0.036\,\mu\text{m}^3$ at 10 min, but decrease to $\approx 0.007\,\mu\text{m}^3$ after 40 min (Figure 3C). This transient increase could correspond to a swelling up of droplets prior to full dispersal caused by amphiphile-motifs attaching to and destabilizing the surface of droplets. By comparison, after addition of control-motifs, droplets increase in size to $\approx 0.07\mu m^3$, in line with droplet coarsening. We could also confirm an initial increase in sphericity followed by a drop back to ≈ 0.4 after addition of amphiphile-motifs (Figure 3C). In contrast, control-motif addition leads to a continuous increase in sphericity to ≈ 0.55. In conclusion, addition of amphiphile-motifs to preformed Y-motif droplets induces a transient increase in volume and sphericity, followed by full droplet dispersal. Adding control-motifs without poly-T extension also leads to an increase in droplet volume and sphericity, whereas the subsequent volume reduction and dispersal do not occur.

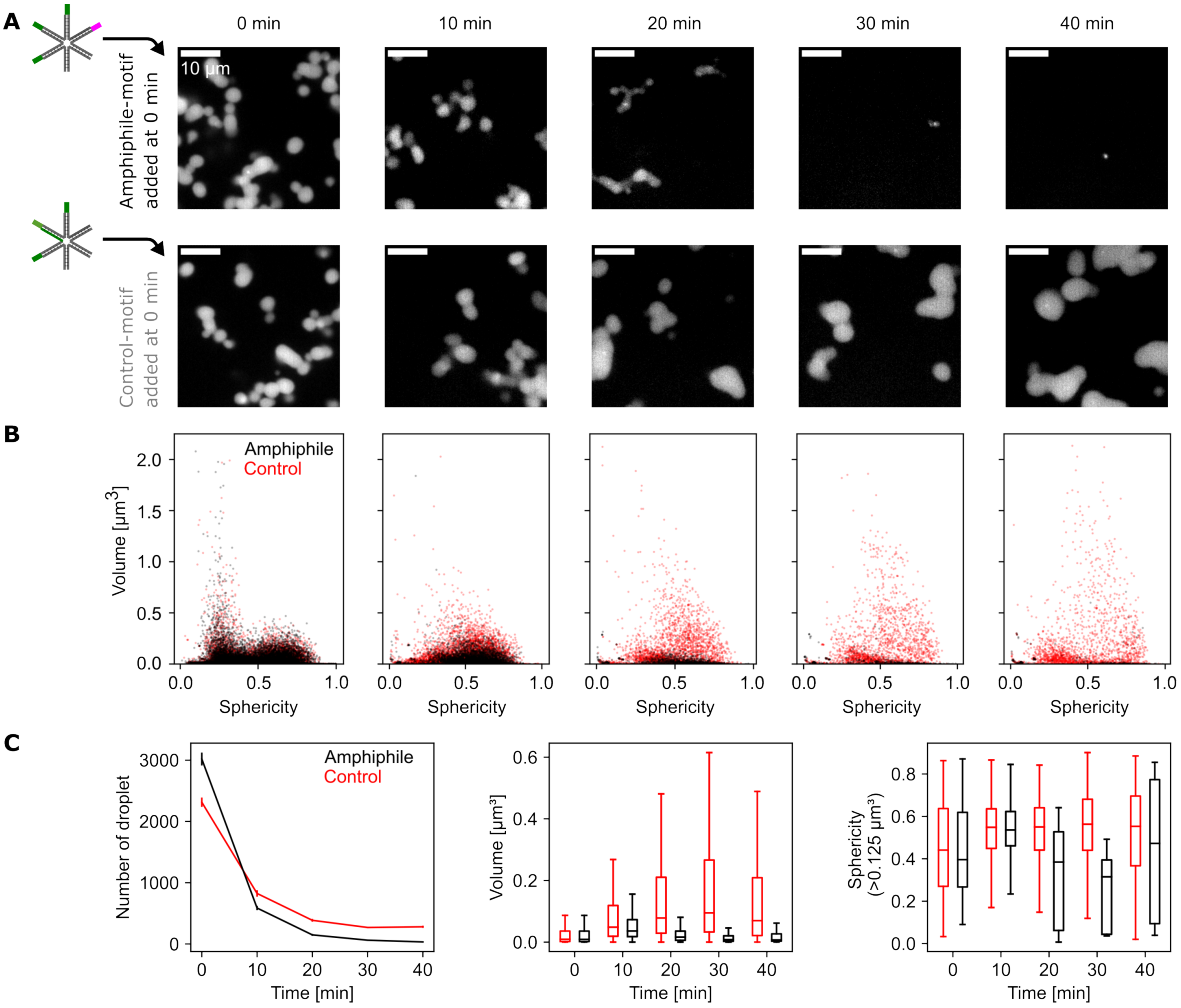

Fig. 3: **Time-course of droplet dispersal upon addition of amphiphile-motifs.** A) Representative confocal microscopy sections showing the distribution of Y-motifs in flow cells prepared at 10-min time intervals after amphiphile-motifs were added to preformed Y-motif droplets (0 min). Several tubes prepared in this manner were maintained at a stable temperature of 50°C, control-motif samples were processed alongside amphiphile-motifs experiments. B) Sphericity-volume distributions obtained from the analysis of confocal images. Three-dimensional analysis was carried out in image stacks (image stacks were acquired at 7 fields of view per sample and time point, data pooled from one experiment. Number of droplets, amphiphile-motif addition: n=21123, 4110, 1044, 437, 239; control-motif addition: n=6191, 5775, 2707, 1890, 1969. C) Time courses of the number of droplets per field of view (mean±SEM, $n = 7$ fields of view per time point), volume of droplets (standard boxplots, all droplet volumes included), and the sphericity of large droplets (volumes $\geq 0.125\,\mu\text{m}^3$ included).

Amphiphile titration experiments mimic the dispersal of RNA polymerase II clusters

Having verified that amphiphile-motifs induce the expected droplet dispersal via a surface effect, we investigated whether they could be used to mimic the dispersal of transcriptional clusters with increasing levels of transcript elongation in zebrafish embryos. To imitate increasing levels of transcript elongation, we prepared mixtures of Y-motifs with increasing concentrations of amphiphile-motifs. Different from our previous time-lapse experiments, Y-motifs and amphiphile-motifs were mixed and then subjected to transient heating to overcome delays in the dispersal of droplets due to slow ripening kinetics (Figure 4A). In line with our previous observations, at all concentrations, amphiphile-motifs colocalized with Y-motif droplets and higher amphiphile concentrations were associated with smaller droplets (Figure 4B). Scatter plots of volume versus sphericity reveal that, with increasing amphiphile concentration, the volume-sphericity distribution undergoes changes similar to Pol II clusters in zebrafish embryos for increasing levels of transcription (Figure 4C). In particular, the transient increase in the percentage of droplets with high volume and high sphericity mirrors the results for Pol II clusters. Furthermore, targeted analyses reveal a good agreement with observations made for Pol II clusters: The droplet number transiently increases, then drops below the value without addition of amphiphile-motifs, as seen for Pol II clusters with increasing levels of transcription (Figure 4D). The droplet volume, similar to the volume of Pol II clusters, does not change appreciably (Figure 4D). A mild decrease in sphericity for high amphiphile-motif concentrations could be observed, which is in line with the solidity decrease seen for Pol II clusters (Figure 4D). The sphericity also shows a slight, transient increase (Figure 4D), an effect that is more clearly visible in the scatter plots (Figure 4C). All observations were also visible in a second repeat of the titration experiment, indicating their reproducibility (Figure S1). Taken together, the changes in Y-motif droplets with increasing amphiphile-motif concentration resemble the changes in Pol II clusters in zebrafish embryos for increasing levels of transcript elongation.

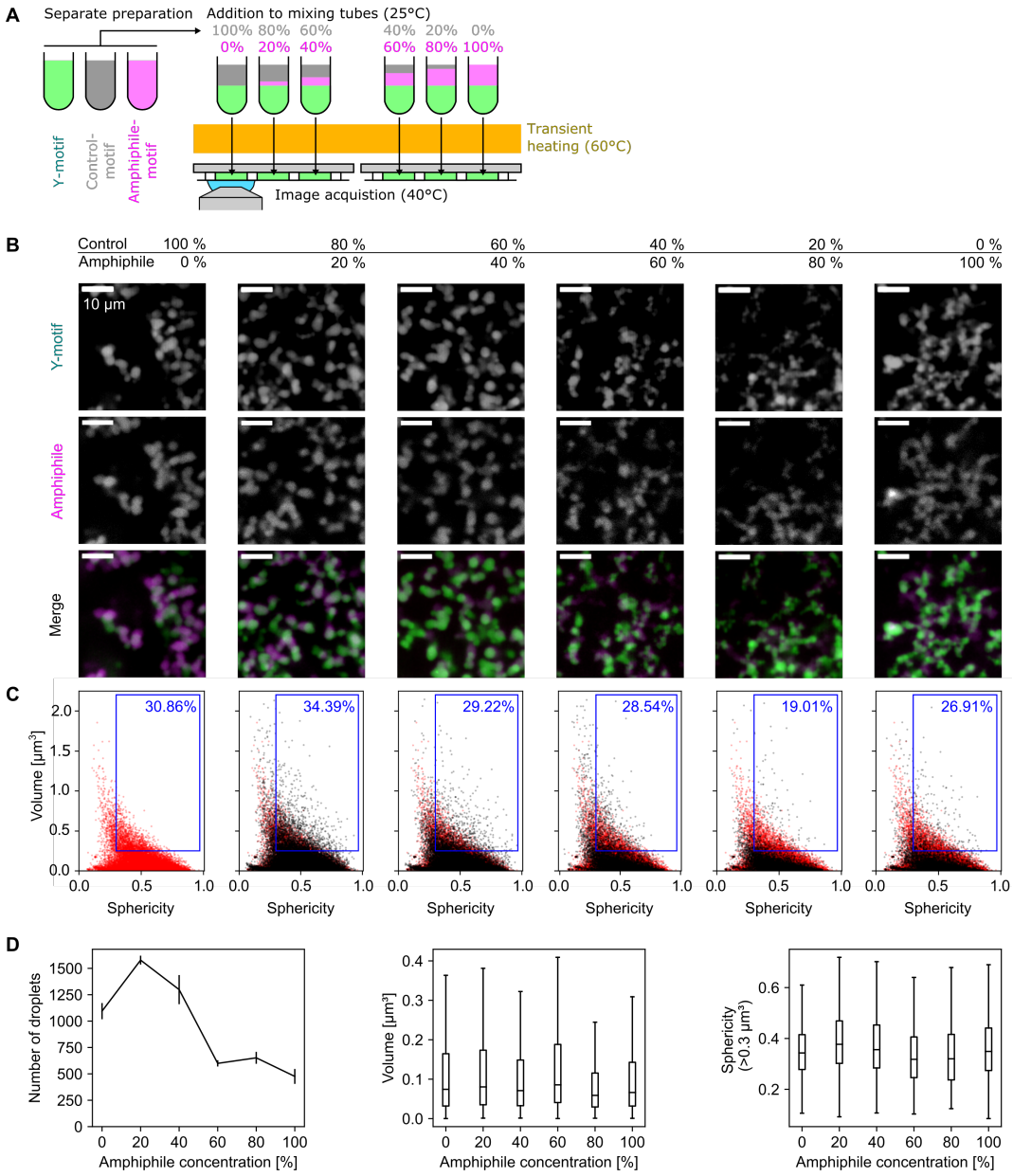

Fig. 4: **Increased amphiphile concentration leads to dispersal of phase-separated droplets.** A) Y-motifs, control-motifs (no poly-T extension), and amphiphile-motifs were separately prepared, mixed at different percentages of amphiphile-motif, transiently heated (60°C), and injected into flow cells for microscopy (ambient temperature 40°C). B) Representative two-color micrographs of Y-motif and amphiphile-motif distributions at different amphiphile-motif concentrations. Micrographs are single confocal sections. C) Sphericity-volume distributions obtained from the analysis of confocal image stacks (image stacks were acquired at up to five fields of view per sample, n=15323, 22091, 18177, 7793, 8477, 6663 droplets, data pooled from $N = 14, 14, 13, 13, 14, 14$ total fields of view pooled from three independent experimental repeats). D) Changes with amphiphile concentration of the number of droplets per field of view (mean±SEM, $n = 14, 14, 13, 13, 14, 14$ fields of view), volume of droplets (standard boxplots, all droplet volumes included), and the sphericity of large droplets (volumes$\geq 0.3\,\mu\text{m}^3$ included).

Simulation of Y-motif droplet dispersal by amphiphile-motifs

Our experimental results suggest that two types of interactions are mainly responsible for the formation and dispersal of Y-motif droplets. Firstly, attractive interactions among Y-motifs and amphiphile-motifs, which lead to Y-motif droplet formation as well as the recruitment of amphiphile-motifs to Y-motif droplets. Secondly, repulsive interactions that are introduced via a repulsive domain added to amphiphile-motifs, leading to repulsion of Y-motifs and other amphiphile-motifs (graphical summary see Figure S2). To assess whether these interactions are indeed sufficient to explain our experimental observations, we implemented according simulations based on Langevin dynamics (Figure 5A). This model coarse-grains motifs into simplified particles with pair-wise interactions that only depend on particle-particle distances. Y-motifs are represented as spherical particles, which interact with other particles of the same kind via a harmonic well potential, meaning that Y-motifs can adhere to each other and form droplets. Amphiphile-motifs are represented as composite particles comprising one "Y-motif-particle" and one "tail particle", which experiences harmonic repulsion from all other particles. This composite particle thus simultaneously experiences attraction to the Y-motif phase via the Y-motif part and repulsion from other particles due to the attached "tail particle". The diffusion constants used are based on the Stokes–Einstein equation for particles with 10 nm and 20 nm radius for Y-motif and tail particle, respectively (Figure 5A). Droplet formation in these simulations is largely determined by the ratio of attractive to repulsive forces, which can be adjusted by increasing the depth of the well-potential that represents attraction while keeping repulsive interaction fixed. Setting this potential depth to $2k_BT$ reproduces the experimentally observed transient increase in the number of droplets with increasing amphiphile-motif concentrations (Figure S3).

To investigate whether this model captures our experimental findings on droplet dispersal upon amphiphile addition, we initialized a simulation with only Y-motifs, which we allowed to proceed until droplets were formed. To this system configuration, containing preformed droplets, equal numbers of either amphiphile-motifs or control-motifs were added. The addition of amphiphile-motifs led to full dispersal of the smaller preformed droplet and prevented further growth of the larger droplet (Figure 5A). Starting from an identical initial configuration with two droplets, the addition of control-motifs resulted in continued growth for both droplets (Figure 5A). Scatter plots of sphericity and droplet size for each case substantiate the impression that only the control simulations allow for droplet growth, whereas small droplets disappear over time in the amphiphile simulation (Figure 5B). Further quantification of the number of droplets per simulation reveals a decrease in number that is more pronounced for the amphiphile-motif case, which is in line with our experimental observations (Figure 5C). Similar to the experiment, addition of control-motifs allows a more pronounced increase in droplet size than the addition of amphiphile-motifs (Figure 5C). Lastly, control-motif addition results in a continuous sphericity increase, whereas addition of amphiphile-motifs led to a transient increase followed by a decrease, as observed in experiments (Figure 5C). Overall, the simulations thus reproduce the time-lapse observations following the addition of amphiphile-motifs as well as control-motifs. One difference is that the median droplet volume after adding amphiphile-motifs only transiently increased in the experiment, but increased continuously in the simulation. A reason for this could be that the volume distributions generated by simulation and experiment are dominated by different effects. Changes in the simulated distribution are dominated by the loss of smaller droplets. As a consequence, the median droplet size remains constantly elevated after an initial increase caused by amphiphile incorporation. In contrast, in the experiment, the smaller droplets that disperse over time are not detected due to the limited resolution of the microscope. The distribution therefore transiently shifts to higher volumes, as larger droplets swell up before splitting and, ultimately, disperse.

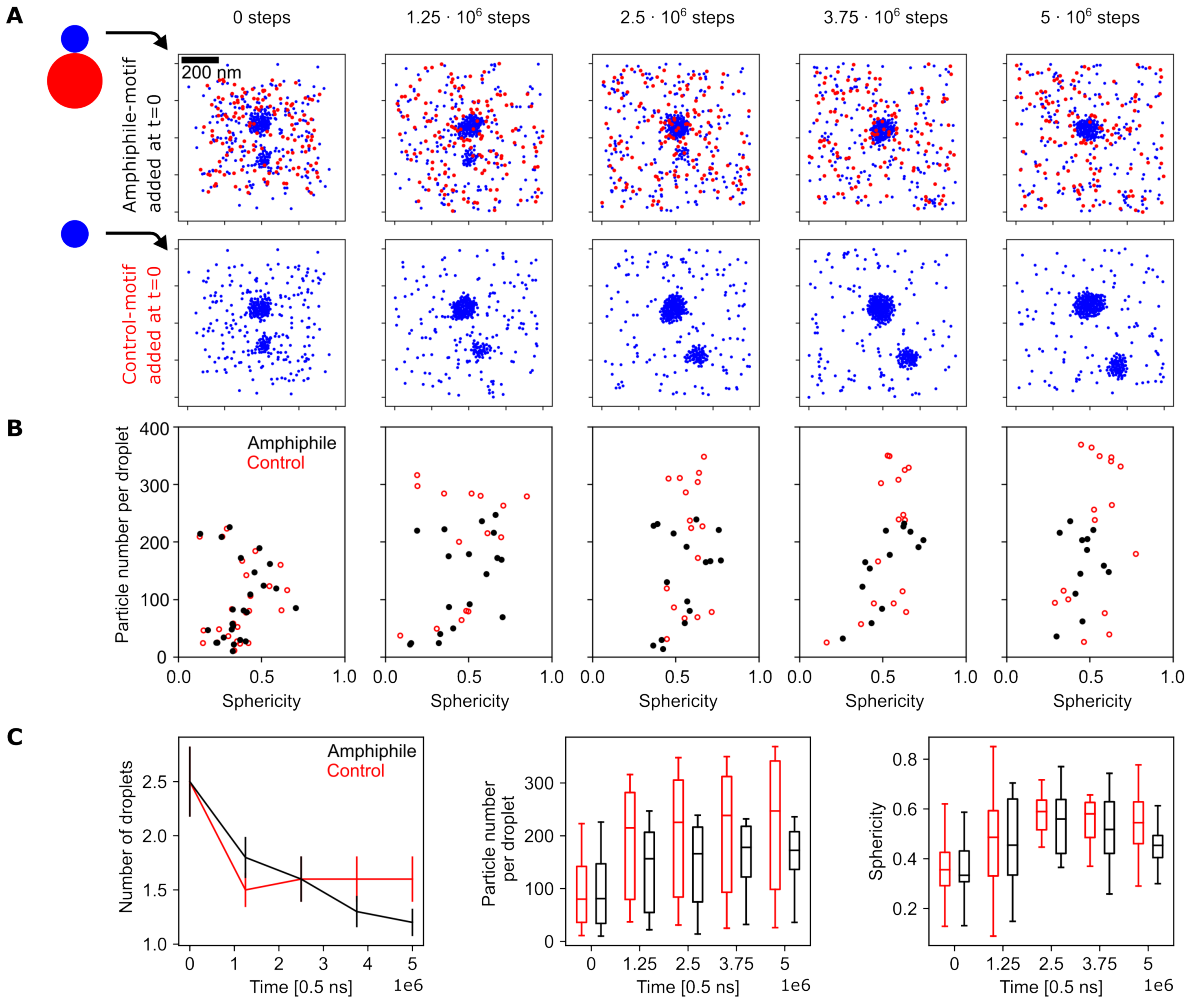

Fig. 5: **Time series of amphiphile-mediated droplet dispersal obtained from interacting-particle simulations** A) To simulate the time-lapse experiment, either amphiphile-motifs or control-motifs were added to a simulation containing preformed Y-motif droplets. The preformed droplets were generated by adding 450 Y-motifs to a simulation box of 1x1x1 μm and simulating for 10^6 steps at a temperature of 60°C. Following this step, 450 additional amphiphiles or Y-motifs serving as control were added at random positions in a way that particle overlaps are prevented. $5 \cdot 10^6$ additional steps at a temperature of 40°C were then carried out. Representative z-slices of 200 nm thickness from both simulation cases are shown. Both simulations started from the same initial configuration. Control motifs were implemented identically to Y-motifs and are also displayed in blue color. B) 10 simulations for each case were used to generate distributions of sphericity versus particle number per droplet. C) The mean number of droplets per simulation and boxplots for particle number per droplet and sphericity are shown for different time points.

Simulated titration reproduces experimental results from transcriptional clusters and Y-motif droplets

Finally, to assess whether our theoretical model can reproduce the dispersal of Y-motif droplets with increasing amphiphile-motif concentration, we simulated a titration experiment with increasing concentrations of amphiphile-motifs (Figure 6A). The volume fractions in the experiments with DNA-nanomotifs can be directly mapped to the particle number fractions in these simulations and the simulations are assigned physical length scales, so that results from simulations can be thoroughly compared to the experiments (Figure 6B). Visually, an increase in amphiphile-motif concentration leads to a more prominent accumulation of amphiphile-motifs on the surface of Y-motif droplets and smaller Y-motif droplets (Figure 6B). Sphericity-volume scatter plots show an increased fraction of large droplets with high sphericity, followed by decrease of this fraction for even higher amphiphile-motif concentrations (Figure 6C). The number of detected droplets first rises and then drops, as seen in the experiments (Figure 6D). The simulations show a notable decrease in droplet size, which was not visible in the experiments (Figure 6 D). When we implemented effects from the limited spatial resolution of the confocal microscope and used an image-based assessment of droplet size instead of particle-counting, the decrease in droplet size largely disappeared, matching our experimental observations (Figure 6D, inset). Similar to our experiments, the sphericity of droplets decreases at higher amphiphile-motif concentrations and a slight increase at intermediate amphiphile-motif concentrations can be seen (Figure 6D). Again, as in the experiments, the changes in sphericity are more evident in the sphericity-volume scatter plots (Figure 6D). In summary, our theoretical model largely captures the observations for increasing concentrations of amphiphile-motifs, and, by extension, for transcriptional clusters with increasing levels of transcription. In particular, a transient increase in droplet number and a transient increase in the fraction of droplets with high volume and sphericity could be observed in all three cases, indicating a stereotypical behaviour.

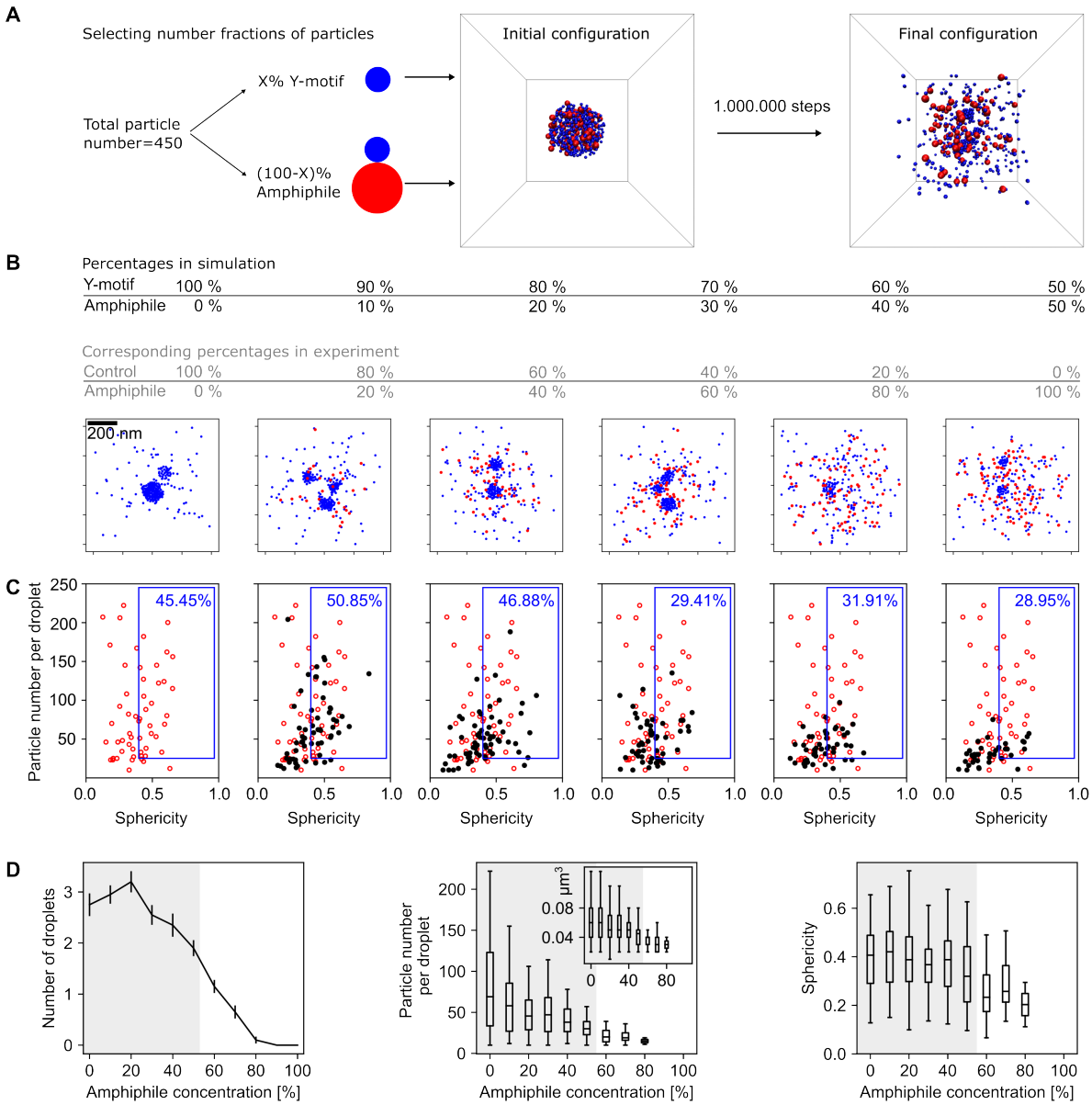

Fig. 6: **Amphiphile titration in interacting-particle simulations.** A) 450 particles in total were used for the titration simulation. The fraction of amphiphile was increased from 0% to 100% in steps of 10%, the remaining fraction comprising of Y-motifs. Initially, all particles were distributed in a spherical volume of 200 nm inside a simulation box of 1x1x1 μm. 10^6 simulation steps were then carried out and the final configuration was evaluated. B) Due to the different methods of assigning percentages (number fractions in the simulation, volume fractions in the experiment), we provide corresponding percentages from the experiment in grey. One example of a z-slice (thickness 200 nm) of the final configuration is shown for each case. C) Distributions of sphericity against particle number per droplet from 20 independent simulations. The blue box contains a percentage of droplets with sphericity higher than 0.4 and more than 25 particles per droplet. D) Mean number of droplets per simulation, boxplots of the particle number per droplet, and boxplots of the sphericity. Grey regions correspond to the range investigated in the experiment. Note that the inset corresponds to droplet volumes obtained after discretizing the simulation box into cubes of 10 nm edge length.

Discussion

In this study, we demonstrate that phase-separating droplets formed purely from synthetic DNA-nanomotifs can be dispersed by increasing concentrations of amphiphilic DNA-nanomotifs in a manner that closely resembles the dispersal of transcriptional clusters in stem cells. The close resemblance, in our understanding, is due to the similarity in the underlying amphiphile-mediated dispersal process, which occurs independent of whether the amphiphile is established by negative charges of thymine or by newly produced RNA transcripts emerging at transcribed genes. For both types of amphiphiles, for low amphiphile levels, rounded-out shapes are energetically favourable, as the localization of amphiphiles to the droplet surface is sufficient to maximise the distance between newly produced poly-T tails or RNA transcripts. For higher amphiphile concentrations, droplets split and ultimately become dispersed beyond the detection limit of our microscope. Our simulations confirm that, indeed, the combination of phase-separating particles with amphiphilic particles is sufficient to explain the observed dispersal. Taken together, these results show how the addition of a relatively simple amphiphilic DNA-nanomotif can be used to control the size of phase-separated droplet compartments or even induce complete dispersal of these compartments. We believe that, in the future, such a biomimetic approach can be extended to other nuclear bodies and gene-regulatory processes to find inspiration for the design of technical or biomedical nanosystems.

Our results support the previously proposed hypothesis that a combination of droplet formation by phase separation and dispersal by increasing influence of an amphiphile is sufficient to produce the most prominent aspects of the dispersal of transcriptional clusters upon transcriptional activation [27]. However, transcriptional clusters exhibit several features that are not reflected in the synthetic DNA-motifs used in our study. Transcription in eukaryotes proceeds via several adjacent compartments at the scale of $\tilde{1}00$ nm, which harbor the consecutive steps of transcription control, transcript elongation, and splicing of the resulting transcripts [38–42]. The ability to implement several, orthogonally interacting DNA-motifs based on different sticky end sequences allows a similar formation of distinct droplet species, whose fusion and separation can be controlled by additional connector motifs [5, 7]. The formation of transcriptional clusters in pluripotent cells involves super-enhancers as condensation surfaces [27–31, 39, 43–45], whereas the Y-motif droplets in our study form without such condensation surfaces. The addition of DNA strands of $\geq$ 10 kb length with affinity for the Y-motifs would be an extension to our system that would mimic the proposed role of super-enhancers as condensation surfaces. Several recent studies address the role of such condensation surfaces in the formation of clusters of transcription factors and Pol II [27, 46, 47]. In contrast to canonical formation of droplets by LLPS, cluster formation by surface condensation can occur below the typical saturation concentration required for droplet formation. Furthermore, surface condensates are limited in size in proportion to the available condensation surface, which also differs from the continuous growth of droplets due to ripening processes as expected by canonical phase separation models. Despite these clear differences between the processes of canonical droplet formation by LLPS and surface condensation, the observed dispersal of condensates by amphiphilic particles in our study is still highly similar in transcriptional clusters, synthetic DNA droplets, and simulations without condensation surfaces. Accordingly, the involvement of condensation surfaces does not seem to impart obvious differences on the process of amphiphile-mediated dispersal, but could be considered in future, more realistic synthetic reimplementations of transcriptional clusters.

A second difference of our synthetic system to actual transcriptional clusters is that amphiphiles are formed at transcribed genes during the ongoing, active process of transcript production [26, 27]. In contrast, the amphiphilic DNA-nanomotifs in our synthetic system are catalytically inactive. On the one hand side, transcribed genes as well as the synthetic amphiphiles are located at the surface of condensates, and the cluster shape changes induced by higher amphiphile levels are comparable. On the other hand, the ongoing synthesis and transport of RNA can distinctly change the stability of transcriptional clusters [27] as well as the mesoscopic organization of different steps of the transcription process as well as chromatin [26, 48, 49]. A feedback from RNA transcript synthesis towards the dispersal of Pol II clusters has also been described on the basis of the electric charge balance between

RNA and other soluble components of the transriptional clusters [50]. This model is in line with our own finding that the addition of poly-A blockers in our droplet experiments can remove the influence of the negatively charged poly-T tails of the amphiphile particles. An accumulation of Pol II on the surface of Yes-associated protein (YAP) droplets has also been observed upon hyperosmotic shock, and precedes droplet dispersal upon transcriptional activation [51]. Considering that Pol II accumulates at the droplet surface already an hour before droplet dispersal, newly produced RNA might again establish the dispersing amphiphilic properties of transcribing Pol II. These studies suggest that, while no obvious discrepancies seem to result from the absence of ongoing RNA synthesis in our analysis, a more realistic reimplementation of transcriptional clusters could take such catalytic processes into consideration.

Our study adds to a growing number of biomimetic systems that use fundamental principles from phase separation biophysics to recreate key aspects of cellular organization and function. For example, reengineered fusion proteins that can be optogenetically induced to phase-separate and targeted to specific genomic loci based on a catalytically inactive Cas9 domain were used to assess the mechanical interaction between phase-separated nuclear bodies and the surrounding chromatin meshwork [52]. A DNA-nanomotif approach similar to the one used in this study was used to construct a DNA segregation module emulating chromosome separation during cell division [7]. Changes to droplet size and number as a function of amphiphile concentration were also observed in a synthetic system using protein amphiphiles comprising an intrinsically disordered region (IDR) fused with a folded domain [18]. In another polymer-based synthetic system, molecular assemblies with distinctly different organization emerge as the system switches between different pathways of assembly depending on the interaction strength between solvent and amphiphile [53]. In conclusion, these examples highlight that amphiphilicity can serve as a theoretical concept and as an addressable control parameter for the size and shape of phase-separated droplets in biological cells as well as synthetic systems.

Methods and Materials

Zebrafish husbandry and collection of embryos

All zebrafish husbandry was performed in accordance with the EU directive 2010/63/EU and German animal protection standards (Tierschutzgesetz §11, Abs. 1, No. 1) and is under supervision of the government of Baden-Württemberg, Regierungspräsidium Karlsruhe, Germany (Aktenzeichen35-9185.64/BH KIT).

Immunofluorescence staining of zebrafish embryo animal caps

Zebrafish embryos in the sphere stage were collected as previously explained [27]. In particular, wild-type adult fish (AB from the Zebrafish International Resource Center, maintained at the European Zebrafish Resource Center) were set up for spontaneous mating, eggs were collected and chorions removed by treatment with pronase. Embryos were maintained in 0.3X Danieau's solution, and transferred into 0.3X Danieau's supplemented with 2% formaldehyde and 0.2% Tween-20 for fixation. Permeabilization was carried out by 15 min exposure to 0.5% Triton X-100 in phosphate-buffered saline (PBS, Dulbeccos's formulation) for 15 min at room temperature. After two washes in PBS with 0.1% Tween-20 (PBST), 30 min of blocking with 4% Bovine Serume Albumin (BSA) in PBST followed. Samples were then incubated at 4°C overnight with primary antibodies against Pol II S2P (Abcam ab193468, rabbit IgG monoclonal, clone EPR18855, dilution 1:300) and Pol II S5P (Active Motif, rat IgG monoclonal, clone 3E8, dilution 1:300) in 4% BSA-PBST. After 3 washes in PBST, the samples were again incubated overnight with secondary antibodies (ThermoFisher, anti-rat polyclonal conjugated with Alexa 594, 1:300; ThermoFisher anti-rabbit polyclonal conjugated with STAR RED 1:300) in 4% BSA-PBST. Samples were washed 3 times in PBST, post-fixed in 2% formaldehyde in PBS for 15 min at room temperature, again washed 3 times in PBST. Mounting was carried out by placing animal caps immersed in non-setting mounting media (VectaShield H-1000) supplemented with 1.6 μM Hoechst

33342 between adhesive strips spaced 2-4 mm apart, which were covered with thickness-selected #1.5 glass cover-slips. The assembled sample was then sealed with nail polish.

Preparation of flow cells on microscope slides

Flow cells were prepared by placing strips of double-sided tape on glass microscope slides to form several channels. To block surfaces for binding, the flow cells were incubated with 2% bovine serum albumin (BSA) for 5 min. After removing the remaining solution with a chemical wipe, the microscope slides were air-dried. Then cover slips were placed on the microscope slides. For imaging, the flow cell channels were filled with sample solution and sealed with silicone grease.

Preparation of DNA-nanomotif suspensions

Oligonucleotide preparation.

Oligonucleotides were purchased from biomers.net and Integrated DNA Technologies (IDT) with purification by standard desalting (unmodified strands) or HPLC (fluorophore-tagged strands). The individual strand sequences were taken from [5] and adapted as detailed in Supplementary Table S1. Individual oligonucleotide preparations were dissolved in 1X TE at 200 μM and stored at -20°C up until preparation of mixtures needed for a given experiment.

Nanomotif formation.

To produce the different nanomotifs (Figure 2A, B), the corresponding DNA-oligomers were separately mixed together in 25 μl of 2X TE with 700 mM NaCl. The solutions were then heated up with a thermocycle (Eppendorf Mastercycler X50) to 85°C for 3 min, before decreasing the temperature at a rate of -1°C/min to 40°C. How the different star motifs affect the Y-droplets was investigated by first preparing all components separately (5.0 μM Y-motif and 1.65 μM star motif), then mixing both parts in equal proportions and heating up to 60°C before decreasing the temperature at a rate of -1°C/min. Annealed nanomotifs were used immediately.

Inhibition of amphiphile with poly-A blocker elements.

Nanomotifs were prepared separately, (10.0 μM Y-motif and 5.0 μM star-motif). Then, 4.44 μM Y-motif and 2.22 μM amphiphile-motif were mixed together with 22.2 μM of a 10-nt poly-A blocker (for sequences see Supplementary Table S1). Control solutions were prepared by the substitution of the poly-A blocker solution with an equivalent amount of water. The samples were heated up to 60°C, then the temperature was decreased at a rate of -1°C/min to 40°C before imaging the samples.

Time-lapse of amphiphile-droplet interaction.

Time-lapse experiments were performed by first preparing 20.0 μM Y-motif and 15.0 μM of amphiphile-motif in separate tubes, then mixing 10.0 μM of the Y-motif solution with 7.5 μM of the amphiphile-motif solution (concentrations in final mixture). The mixture was then added to preheated (40°C) flow cells and imaged at 40°C for up to 4 h.

Time-course of amphiphile-droplet interaction with incubation in a thermocycler.

The time-lapse experiments were repeated at 50°C, assuming that the nanomotifs reorganize faster at elevated temperature. Here, 10.0 μM of Y-motif and 15.0 μM of amphiphile-motif and control-motif were prepared separately, before mixing 5.0 μM Y-motif and 7.5 μM amphiphile-motif or control-motif together (concentrations in final mixture). Several tubes were prepared and incubated at 50°C in a thermocycler. Every 10 min, an amphiphile-motif and a control-motif sample were retrieved from the thermocycler and injected into preheated flow cells (40°C) for imaging (ambient temperature 40°C).

Titration of amphiphile-motifs.

Titration experiments were conducted by preparing 30.0 μM of Y-motifs and 22.5 μM of amphiphile-motifs and control-motifs in 3 separate tubes. Then, 6 tubes of 15 μM Y-motif and 11.25 μM amphiphile and control-motif were mixed together. In the first tube, only 11.25 μM of control-motif were added. In the following tubes, the control-motif was replaced with amphiphile-motifs in 20%-steps, so that the last tube only contained amphiphile-motifs and Y-motifs. These tubes were then heated up to

60°C and cooled down at a rate of -1°C/min to 40°C. For imaging, the different samples were injected in prewarmed flow cells (40°C) and imaged at 40°C.

Imaging procedure Samples were visualized using an instant structured illumination microscope (iSIM) from VisiTech. Before injection, flow cells were heated up to 40°C. Microscopy of the samples was carried out in a heated microscope stage enclosure at a temperature of 40°C.

Microscopy and image analysis

Zebrafish embryos

Zebrafish embryos: Confocal microscopy images were obtained using a VisiTech iSIM microscope, which is a commercial implementation of a microscope based on the the instant-SIM principle [37]. The microscope is based on a Nikon Eclipse Ti2 microsope body. A motorized correction collar oil immersion objective (CFI SR HP Apo TIRF 100XAC Oil, NA 1.49) was used. Images were acquired with a single ORCA-Flash4.0 V3 camera with sequential acquisition of color channels for maximal positional accuracy and minimal cross-talk. To limit the analysis to conventional gene and enhancer loci, nuclei with visible miR-430-associated foci were excluded from the data set [54–56].

The analysis of fluorescence intensities and shapes of Pol II clusters was carried out following our previous work [27], using MatLab for analysis and the Open Microscopy Environment bioformats plugin for data import [57]. In brief, a two-step segmentation pipeline was applied, first segmenting cell nuclei by Otsu-thresholding of the DNA-channel, followed by robust background threshold segmentation of Pol II clusters from the Pol II Figure channel in each detected nucleus. For each detected cluster, the geometric characteristics volume and sphericity and the mean intensities in the Pol II S5P and the Pol II S2P channel were calculated under consideration of the 3D-shape segmentation mask. Mean intensities were normalized against the median intensity of the containing nucleus to compensate for variability in sample staining and image acquisition between different nuclei and samples. Sphericity was calculated as

$$36\pi V^2/S^3,$$

where V is the volume and S the surface area of a given 3D object

The raw data and the image analysis code for Figure 1 is deposited on Zenodo: `https://doi.org/10.5281/zenodo.5242771`

Nanomotif suspensions:

Nanomotifs were imaged using a water immersion objective (Apo LWD 40x WI λS DIC N2, NA 1.15). Images were recorded using a single Dual Flash4.0 camera with sequential acquisition.

The images were further processed with the software Fiji [58]. Raw images containing the droplets formed by Y-motifs were resliced in the z-axis to generate cubic voxels and then filtered using Gaussian Blur 3D with the parameters σ = 2,2,2 pixels for x, y, and z, respectively. To obtain image data for the volume, sphericity, and elongation of the detected droplets, the plugin MorphoLibJ was used [59]. Images were processed with the "Morphological Segmentation" tool as object images with the gradient type "Morphological", gradient radius = 2 and a tolerance = 100. Images were displayed in the "Catchment basins" format. The background was removed by using the command "Remove Largest Object". Images were further analyzed using the tools "Analyse Regions 3D" for the volume and sphericity (surface area method = Crofton (13 dirs.), Euler connectivity = 6).

The raw data and the image analysis code is deposited on Zenodo.

Comparison of different amphiphiles (Figure 2B): `https://doi.org/10.5281/zenodo.7572656`

Blocking of poly-T amphiphiles (Figure 2C): `https://doi.org/10.5281/zenodo.7572624`

Continuous time-lapse on the microscope, 40° (Figure 2E): `https://doi.org/10.5281/zenodo.7572182`

Manual time-lapse, 50° (Figure 3A-C): `https://doi.org/10.5281/zenodo.7572230`

Titration poly-T amphiphile (Figure 4B-D) `https://doi.org/10.5281/zenodo.7573452`

Theoretical model

Interacting-particle dynamics in ReaDDy

Langevin dynamics is a common approach to describe particles subject to both deterministic forces in a Newtonian sense and stochastic forces that result in Brownian motion. In the overdamped limit, particle motion is determined by a stochastic differential equation called Langevin equation:

$$\frac{d\vec{x}}{dt} = -D\frac{\nabla V(\vec{x})}{k_B T} + \eta(t) \ . \tag{1}$$

The particle position is denoted by $\vec{x}$, the diffusion constant by D, the thermal energy by $k_B T$ and a delta-correlated noise term by η. Interactions are summed up in the potential V.

ReaDDy (short for Reaction Diffusion Dynamics) is a software package capable of numerically integrating the Langevin equation (1) for individual particles. Importantly, it also allows the user to include various potentials for interactions between the particles and chemical reactions that can convert, create, or delete particles. This kind of simulation is often referred to as interacting-particle reaction dynamics (iPRD) and has proven versatile enough to model and simulate a variety of biochemical systems. ReaDDy, in version 2.0.12, was used for all simulations based on Langevin dynamics. A more in-depth introduction to ReaDDy can be found in [60].

The Euler-Maruyama method is used to integrate the Langevin equation. The evolution from a position $\vec{x}(t)$ to $\vec{x}(t+dt)$ can be written as:

$$\vec{x}(t+dt) = \vec{x}(t) + \frac{D}{k_B T}\vec{F}(t)\,dt + \sqrt{Ddt}\eta \ , \tag{2}$$

where the effects of external forces and interaction forces with other particles are summed up in $\vec{F}$:

$$\vec{F} = -\nabla\left(\sum_{external} U_{ext} + \sum_{interactions} U_{int}\right) \ . \tag{3}$$

A variety of potentials can be used to model inclusion or exclusion effects and attraction or repulsion between particles. Examples include Lennard-Jones or harmonic pair potentials, spherical barriers or inclusion potentials. A detailed summary can be found on the website of ReaDDy (`https://readdy.github.io/system.html#potentials`).

ReaDDy is accessible via a Python interface, however, the core functionality is written in C++. This way, the user benefits from Python's accessibility without sacrificing optimisation for speed.

Parameters of simulation

The droplet simulation is a coarse-scale, effective model of the DNA-nanomotif system. Our aim was to find a parameter space for particle interaction that reproduces the experimental results. Particle concentrations and sizes are thus not directly comparable to the DNA-system.

Our model for the Y-motif is a spherical particle with diffusion constant $D_y = 0.0352$ nm^2/ns. Interaction with other Y-motifs is defined by a harmonic well potential:

$$\begin{aligned}
V &= \frac{1}{2}k_{wp}(d-r_0)^2 - e, \text{ if } d < r_0 \ , \\
V &= \frac{e}{2}\left(\frac{r_c - r_0}{2}\right)^{-2}(d-r_0)^2 - e, \text{ if } r_0 \le d < r_0 + \frac{r_c - r_0}{2} \ , \\
V &= -\frac{e}{2}\left(\frac{r_c - r_0}{2}\right)^{-2}(d-r_c)^2 \ , \text{ if } r_0 + \frac{r_c - r_0}{2} \le d < r_c \ , \\
V &= 0, \text{ otherwise} \ , \\
d &= \sqrt{\vec{x_1}^2 - \vec{x_2}^2} \ .
\end{aligned} \tag{4}$$

After testing various parameter settings, we decided to use the following for our simulations:

- spring constant of repulsive part: $k_{wp} = 10^{-20}$ J/nm^2
- depth of well: $e = 2 \cdot k_B T$
- position of minimum: $r_0 = 20$ nm
- cut-off distance: $r_c = 30$ nm

The amphiphile particle comprises of one particle identical to the Y-motif model and one "tail particle" that is repulsed by all other particles via a harmonic potential:

$$\begin{aligned} V = \frac{1}{2} k_{hr} \left(d - r_c\right)^2 , \text{ if } d < r_0 \ , \\ V = 0, \text{ otherwise } , \\ d = \sqrt{\vec{x_1}^2 - \vec{x_2}^2} \ . \end{aligned} \tag{5}$$

The following parameters were used:

- spring constant: $k_{hr} = 10^{-20}$ J/nm^2
- cut-off distance: $r_c = 30$ nm

The diffusion constant of the "tail particle" was set to $D_y = 0.0175$ nm^2/ns to model a larger effective volume.

A bond potential defines the interaction between the two sub-particles of our amphiphile model:

$$\begin{aligned} V = k_b \left(d - r_0\right)^2 \ , \\ d = \sqrt{\vec{x_1}^2 - \vec{x_2}^2} \ . \end{aligned} \tag{6}$$

Here, we used the following parameters:

- spring constant: $k_{hr} = 10^{-20}$ J/nm^2
- minimum distance: $r_0 = 31$ nm

All particles are also subject to an inclusion potential defined by:

$$\begin{aligned} V = \sum_{i=1}^{d} \frac{1}{2} k_{bp} d \left(\vec{x}_i, C_i\right)^2, \text{ if } \vec{x}_i \in C_i \ , \\ V = 0, \text{ otherwise } . \end{aligned} \tag{7}$$

The term $d\left(\vec{x}_i, C_i\right)^2$ represents the shortest distance between the particle position $\vec{x_i}$ and the boundary of a cube $C_i = [origin_i, origin_i + extent_i]$.

We used the following parameters:

- spring constant: $k_{bp} = 10^{-20}$ J/nm^2
- extent of box = 800 nm

The box was centered in a simulation volume of extension 1x1x1 μm.

Simulation of time series

Simulations for the time series comprised of two steps: In the first step, 450 Y-motifs were randomly placed in a spherical volume of radius 200 nm and simulated for 10^6 time steps of 0.5 ns and 60°C. The final configuration containing preformed droplets was used for the second step. Here, 450 additional Y-motifs (as control case) or amphiphile-motifs were randomly added into a volume of 0.8x0.8x0.8 μm, without creating particle overlaps. The system was then simulated for $5 \cdot 10^6$ steps of 0.5 ns and a reduced temperature of 40°C. This process was repeated for 10 independent simulations, using the standard interaction parameters defined above.

Simulation of titration

Simulations for the titration split 450 particles between the models for Y-motif and amphiphile-motif. The amphiphile percentage was increased from 0% to 100% in steps of 10%. 20 independent simulations for each case were produced containing 10^6 time steps of 0.5 nm at a temperature of 60°C. Initially, particles were randomly distributed in a spherical volume of radius 200 nm. Interaction parameters were identical to the ones discussed earlier.

Detection and evaluation of simulated droplets

Droplets in the simulations were detected by using the DB scan algorithm as implemented in the python package scikit-learn (version 1.1.2). If not specified otherwise, a minimum sample number of 10 and a maximum distance of 40 nm between particles were used.

As a proxy for the volume of each droplet, the number of particles per droplet was calculated. Alternatively, we discretized the simulation box into cubes of 10 nm edge length and counted the number of filled boxes for each droplet. This approach introduces a limited resolution, as one voxel can contain multiple particles and structure is not resolved for scales smaller than the box length.

Sphericity was calculated by using the python package jakteristics in version 0.5.0 (see `https://github.com/jakarto3d/jakteristics`) which calculates the sphericity of a point cloud as ratio between the largest and the smallest eigenvector.

Acknowledgements

X.T., A.G., M.S., and L.H. are supported by the Helmholtz Program Natural, Artificial, and Cognitive Information Processing (NACIP). X.T. and L.H. received seed funding from the KIT Center Materials for Life Sciencees and Technology (MaTeLiS). M.P.T and K.G received funding by the Federal Ministry of Education and Research (BMBF) and the Ministry of Science Baden-Württemberg within the framework of the Excellence Strategy of the Federal and State Governments of Germany and the Max Planck Society. R.C. and V.Z. were supported by the "Life?" initiative of the Volkswagen Stiftung.

References

[1] L.-P. Bergeron-Sandoval, N. Safaee, and S. W. Michnick. "Mechanisms and Consequences of Macromolecular Phase Separation". In: *Cell* 165.5 (2016), pp. 1067–1079.

[2] Y. Shin and C. P. Brangwynne. "Liquid phase condensation in cell physiology and disease". In: *Science* 357.6357 (2017), eaaf4382.

[3] A. S. Lyon, W. B. Peeples, and M. K. Rosen. "A framework for understanding the functions of biomolecular condensates across scales". In: *Nature Reviews Molecular Cell Biology* 22.3 (2021), pp. 215–235.

[4] H. Udono et al. "DNA Droplets: Intelligent, Dynamic Fluid". In: *Advanced Biology* (2022), p. 2200180.

[5] Y. Sato, T. Sakamoto, and M. Takinoue. "Sequence-based engineering of dynamic functions of micrometer-sized DNA droplets". In: *Science Advances* 6 (2020), eaba3471.

[6] B. J. Jeon, D. T. Nguyen, and O. A. Saleh. "Sequence-Controlled Adhesion and Microemulsification in a Two-Phase System of DNA Liquid Droplets". In: *Journal of Physical Chemistry B* 124.40 (2020), pp. 8888–8895.

[7] M. P. Tran et al. "A DNA Segregation Module for Synthetic Cells". In: *Small* 2202711 (2022), p. 2202711.

[8] J. Gong et al. "Computational DNA Droplets Recognizing miRNA Sequence Inputs Based on Liquid–Liquid Phase Separation". In: *Advanced Functional Materials* 32 (2022), p. 2202322.

[9] S. Do et al. "Engineering DNA-based synthetic condensates with programmable material properties, compositions, and functionalities". In: *Science Advances* 8.41 (2022), eabj1771.

[10] J. Klier et al. "Properties and Applications of Microemulsions". In: *Advanced Materials* 12.23 (2000), pp. 1751–1757.

[11] E. M. Hildebrand and J. Dekker. "Mechanisms and Functions of Chromosome Compartmentalization". In: *Trends in Biochemical Sciences* 45.5 (2020), pp. 385–396.

[12] D. Zwicker, A. A. Hyman, and F. Jülicher. "Suppression of Ostwald ripening in active emulsions". In: *Physical Review E* 92.1 (2015), p. 012317.

[13] D. Michieletto et al. "Nonequilibrium theory of epigenomic microphase separation in the cell nucleus". In: *Physical Review Letters* 123.22 (2019), p. 228101.

[14] A. Narayanan et al. "A first order phase transition mechanism underlies protein aggregation in mammalian cells". In: *eLife* 8 (2019), e39695.

[15] J. Berry et al. "RNA transcription modulates phase transition-driven nuclear body assembly". In: *Proceedings of the National Academy of Sciences USA* 112.38 (2015), E5237–E5245.

[16] D. Zwicker et al. "Centrosomes are autocatalytic droplets of pericentriolar material organized by centrioles". In: *Proceedings of the National Academy of Sciences USA* 111.26 (2014), E2636–E2645.

[17] R. G. Larson, L. E. Scriven, and H. T. Davis. "Monte Carlo simulation of model amphiphile-oil–water systems". In: *Journal of Chemical Physics* 83.5 (1985), pp. 2411–2420.

[18] F. M. Kelley et al. "Amphiphilic proteins coassemble into multiphasic condensates and act as biomolecular surfactants". In: *Proceedings of the National Academy of Sciences USA* 118.51 (2021), e2109967118.

[19] N. Samanta et al. "Sequestration of Proteins in Stress Granules Relies on the In-Cell but Not the In Vitro Folding Stability". In: *Journal of the American Chemical Society* (2021).

[20] S. Cuylen et al. "Ki-67 acts as a biological surfactant to disperse mitotic chromosomes". In: *Nature* 535.7611 (2016), pp. 308–312.

[21] M. A. Ricci et al. "Chromatin Fibers Are Formed by Heterogeneous Groups of Nucleosomes In Vivo". In: *Cell* 160.6 (2015), pp. 1145–1158.

[22] T. Nozaki et al. "Dynamic Organization of Chromatin Domains Revealed by Super-Resolution Live-Cell Imaging". In: *Molecular Cell* 67.2 (2017), 282–293.e7.

[23] S. S. Ashwin et al. "Organization of fast and slow chromatin revealed by single-nucleosome dynamics". In: *Proceedings of the National Academy of Sciences USA* 116.40 (2019), pp. 19939–19944.

[24] B. Bintu et al. "Super-resolution chromatin tracing reveals domains and cooperative interactions in single cells". In: *Science* 362.6413 (2018), eaau1783.

[25] Q. Szabo et al. "TADs are 3D structural units of higher-order chromosome organization in Drosophila". In: *Science Advances* 4 (2018), eaar8082.

[26] L. Hilbert et al. "Transcription organizes euchromatin via microphase separation". In: *Nature Communications* 12 (2021), p. 1360.

[27] A. Pancholi et al. "RNA polymerase II clusters form in line with surface condensation on regulatory chromatin". In: *Molecular Systems Biology* 17 (2021), e10272.

[28] W.-K. Cho et al. "Mediator and RNA polymerase II clusters associate in transcription-dependent condensates". In: *Science* 361 (2018), pp. 412–415.

[29] Y. E. Guo et al. "Pol II phosphorylation regulates a switch between transcriptional and splicing condensates". In: *Nature* 572 (2019), pp. 543–548.

[30] B. R. Sabari et al. "Coactivator condensation at super-enhancers links phase separation and gene control". In: *Science* 361 (2018), eaar3958.

[31] B. A. Gibson et al. "Organization of Chromatin by Intrinsic and Regulated Phase Separation". In: *Cell* 179.2 (2019), 470–484.e21.

[32] K. Shrinivas et al. "Enhancer Features that Drive Formation of Transcriptional Condensates". In: *Molecular Cell* 75.3 (2019), pp. 549–561.

[33] M. Boehning et al. "RNA polymerase II clustering through carboxy-terminal domain phase separation". In: *Nature Structural and Molecular Biology* 25.9 (2018), pp. 833–840.

[34] W. Shao et al. "Phase separation of RNA-binding protein promotes polymerase binding and transcription". In: *Nature Chemical Biology* 18.1 (2022), pp. 70–80.

[35] H. Lyons et al. "Functional partitioning of transcriptional regulators by patterned charge blocks." In: *Cell* 186.2 (2023), pp. 327–345.

[36] H. Hajiabadi et al. "Deep-learning microscopy image reconstruction with quality control reveals second-scale rearrangements in RNA polymerase II clusters". In: *PNAS Nexus* 1.3 (2022), pgac065.

[37] A. G. York et al. "Instant super-resolution imaging in live cells and embryos via analog image processing". In: *Nature Methods* 10.11 (2013), pp. 1122–1126.

[38] J. Li et al. "Single-Molecule Nanoscopy Elucidates RNA Polymerase II Transcription at Single Genes in Live Cells". In: *Cell* 178.2 (2019), 491–506.e28.

[39] J. Li et al. "Single-gene imaging links genome topology, promoter–enhancer communication and transcription control". In: *Nature Structural and Molecular Biology* 27.11 (2020), pp. 1032–1040.

[40] L. S. Forero-Quintero et al. "Live-cell imaging reveals the spatiotemporal organization of endogenous RNA polymerase II phosphorylation at a single gene". In: *Nature Communications* 12 (2021), p. 3158.

[41] H. Ohishi et al. "STREAMING-tag system reveals spatiotemporal relationships between transcriptional regulatory factors and transcriptional activity". In: *Nature Communications* 13 (2022), p. 7672.

[42] P. Cramer. "Organization and regulation of gene transcription". In: *Nature* 573.7772 (2019), pp. 45–54.

[43] S. Chong et al. "Imaging dynamic and selective low-complexity domain interactions that control gene transcription". In: *Science* 361.6400 (2018), eaar2555.

[44] D. McSwiggen et al. "Evidence for DNA-mediated nuclear compartmentalization distinct from phase separation". In: *eLife* 8 (2019), e47098.

[45] J. Trojanowski et al. "Transcription activation is enhanced by multivalent interactions independent of phase separation". In: *Molecular Cell* 82.10 (2022), pp. 1878–1893.

[46] J. A. Morin et al. "Sequence-dependent surface condensation of a pioneer transcription factor on DNA". In: *Nature Physics* 18.3 (2022), pp. 271–276.

[47] T. Quail et al. "Force generation by protein–DNA co-condensation". In: *Nature Physics* 17 (2021), pp. 1007–1012.

[48] R. Nagashima et al. "Single nucleosome imaging reveals loose genome chromatin networks via active RNA polymerase II". In: *The Journal of Cell Biology* 218.5 (2019), jcb.201811090.

[49] M. Feric et al. "Mesoscale structure-function relationships in mitochondrial transcriptional condensates". In: *Proceedings of the National Academy of Sciences USA* 119.41 (2022), e2207303119.

[50] J. E. Henninger et al. "RNA-mediated feedback control of transcriptional condensates". In: *Cell* 184.1 (2021), pp. 207–225.

[51] D. Cai et al. "Phase separation of YAP reorganizes genome topology for long-term YAP target gene expression". In: *Nature Cell Biology* 21.12 (2019), pp. 1578–1589.

[52] Y. Shin et al. "Liquid nuclear condensates mechanically sense and restructure the genome". In: *Cell* 175.6 (2018), pp. 1481–1491.

[53] A. Ianiro et al. "Liquid–liquid phase separation during amphiphilic self-assembly". In: *Nature Chemistry* 11.4 (2019), pp. 320–328.

[54] Y. Sato et al. "Histone H3K27 acetylation precedes active transcription during zebrafish zygotic genome activation as revealed by live-cell analysis". In: *Development* 146.19 (2019), dev179127.

[55] S. H. Chan et al. "Brd4 and P300 Confer Transcriptional Competency during Zygotic Genome Activation". In: *Developmental Cell* 49.6 (2019), 867–881.e8.

[56] Y. Hadzhiev et al. "A cell cycle-coordinated Polymerase II transcription compartment encompasses gene expression before global genome activation". In: *Nature Communications* 10.1 (2019), p. 691.

[57] I. G. Goldberg et al. "The Open Microscopy Environment (OME) Data Model and XML file: open tools for informatics and quantitative analysis in biological imaging". In: *Genome Biology* 6.5 (2005), R47.

[58] J. Schindelin et al. "Fiji: an open-source platform for biological-image analysis". In: *Nature Methods* 9.7 (2012), pp. 676–682.

[59] D. Legland, I. Arganda-Carreras, and P. Andrey. "MorphoLibJ: integrated library and plugins for mathematical morphology with ImageJ". In: *Bioinformatics* 32.22 (2016), pp. 3532–3534.

[60] M. Hoffmann, C. Fröhner, and F. Noé. "ReaDDy 2: Fast and flexible software framework for interacting-particle reaction dynamics". In: *PLoS Computational Biology* 15.2 (2019), e1006830.

Supplementary Information

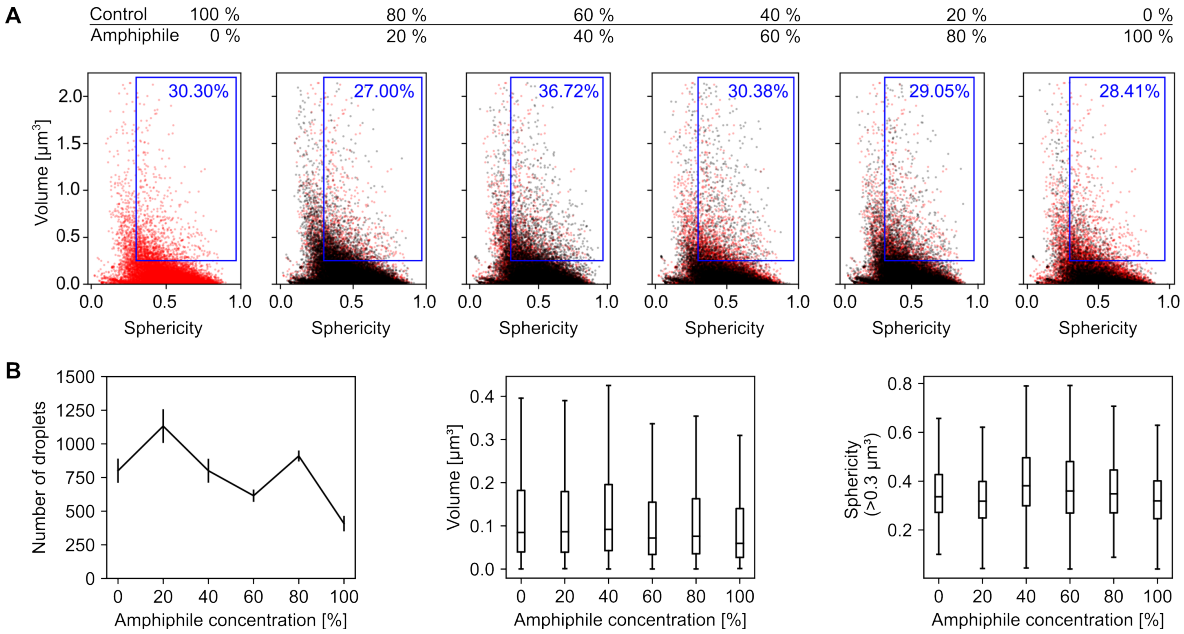

Fig. S1: **Repeat of the amphiphile titration experiment** A repeat of the titration experiment described in figure 4 resulted in similar behaviour.Y-motifs, control motifs (no poly-T extension), and amphiphile-motifs were separately prepared, mixed at different percentages of amphiphile motif, transiently heated (60°C), and injected into flow cells for microscopy (ambient temperature 40°C). As the volume fraction of amphiphile increases, the number of droplets and the percentage of larger droplets with high sphericity transiently increases. A) Sphericity-volume distributions obtained from the analysis of confocal image stacks (image stacks were acquired at up to five fields of view per sample, n=$11206, 14718, 11207, 8609, 12740, 5708$ droplets, data pooled from $N = 14, 14, 13, 13, 14, 14$ total fields of view pooled from three independent experimental repeats). B) Changes with amphiphile concentration of the number of droplets per field of view (mean±SEM, $n = 14, 13, 14, 14, 14, 14$ fields of view), volume of droplets (standard boxplots, all droplet volumes included), and the sphericity of large droplets (volumes larger than 0.3 $\mu\,\mathrm{m}^3$ included).

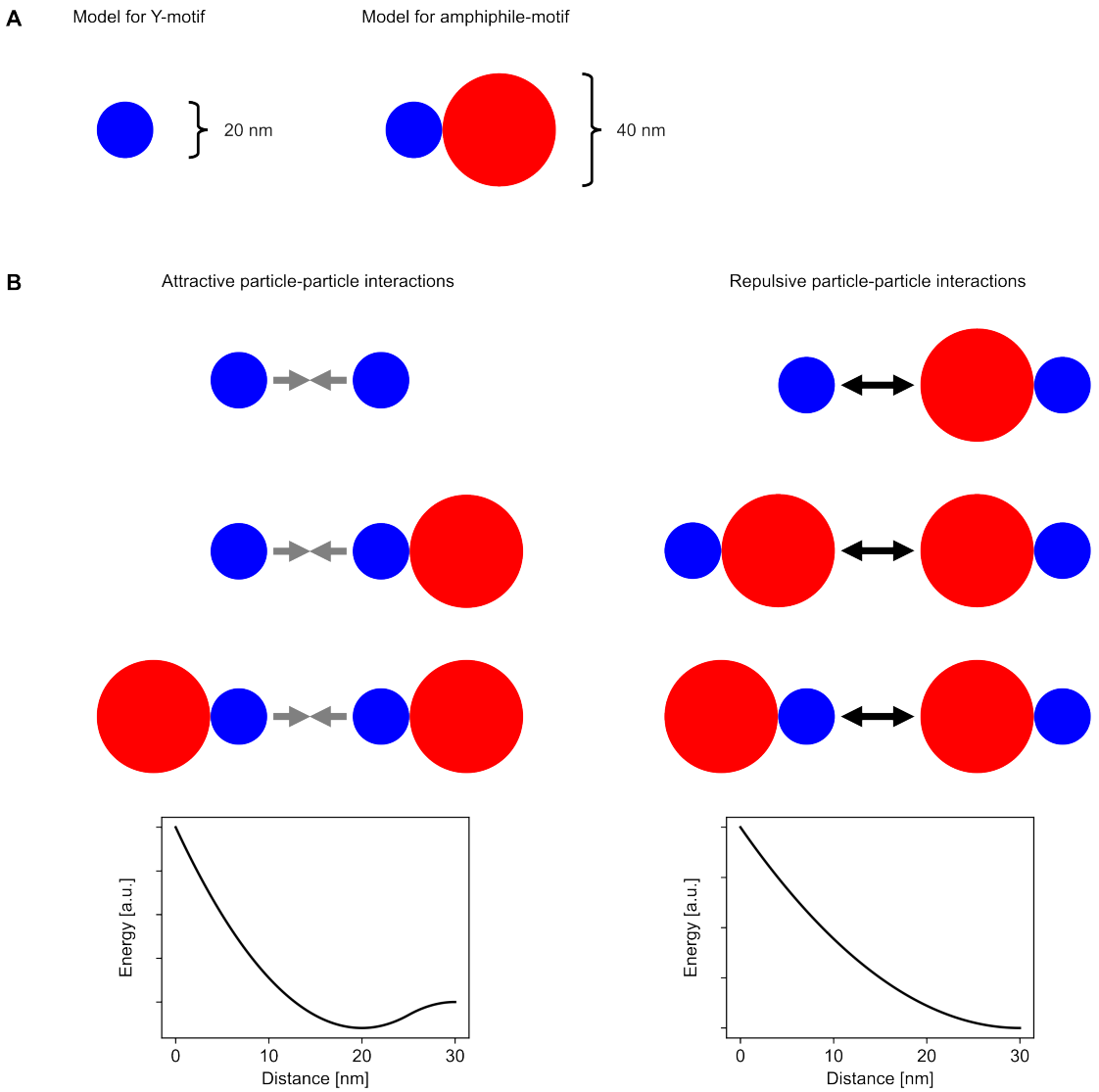

Fig. S2: **Summary of sizes and interaction parameters used for interacting-particle simulations.** A) To-scale drawing of the two types of particles used in the simulation. B) Overview of attractive and repulsive particle interactions, displayed with interaction potentials that implement these interactions in the ReaDDy framework. For better visualisation, the energy axis uses arbitrary units and is not drawn to scale.

Tab. S1: Strand names and sequences of nanomotifs

Strand name	Sequence (5'-3')
Y-1_8	GCTCGAGCCAGTGAGGACGGAAGTTTGTCGTAGCATCGCACC
Y-2_8	GCTCGAGCCAACCACGCCTGTCCATTACTTCCGTCCTCACTG
Y-3_8	GCTCGAGCGGTGCGATGCTACGACTTTGGACAGGCGTGGTTG
Y-2_Atto488	[Atto488]-CAACCACGCCTGTCCATTACTTCCGTCCTCACTG
S-1_0	GCTGGACTAACGGAACGGTTAGTCAGGTATGCCAGCAC
S-2_0	CTCAGAGAGGTGACAGCATTCCGTTCCGTTAGTCCAGC
S-3_0	CCATGGTCCCAAGTGATGTTTGCTGTCACCTCTCTGAG
S-4_8	GCTCGAGCCGGCGCTGTAAATTTGCGTTCATCACTTGGGACCATGG
S-5_8	GCTCGAGCCAGACGTCACTCTCCAACTTCGCAAATTTACAGCGCCG
S-6_8	GCTCGAGCGTGCTGGCATACCTGACTTTGTTGGAGAGTGACGTCTG
S-2_Atto647N	[Atto647N]-CTCAGAGAGGTGACAGCATTCCGTTCCGTTAGTCCAGC
S-1_Phosphate	[Phosphate]-GCTGGACTAACGGAACGGTTAGTCAGGTATGCCAGCAC
S-1_Poly-T	TTTT

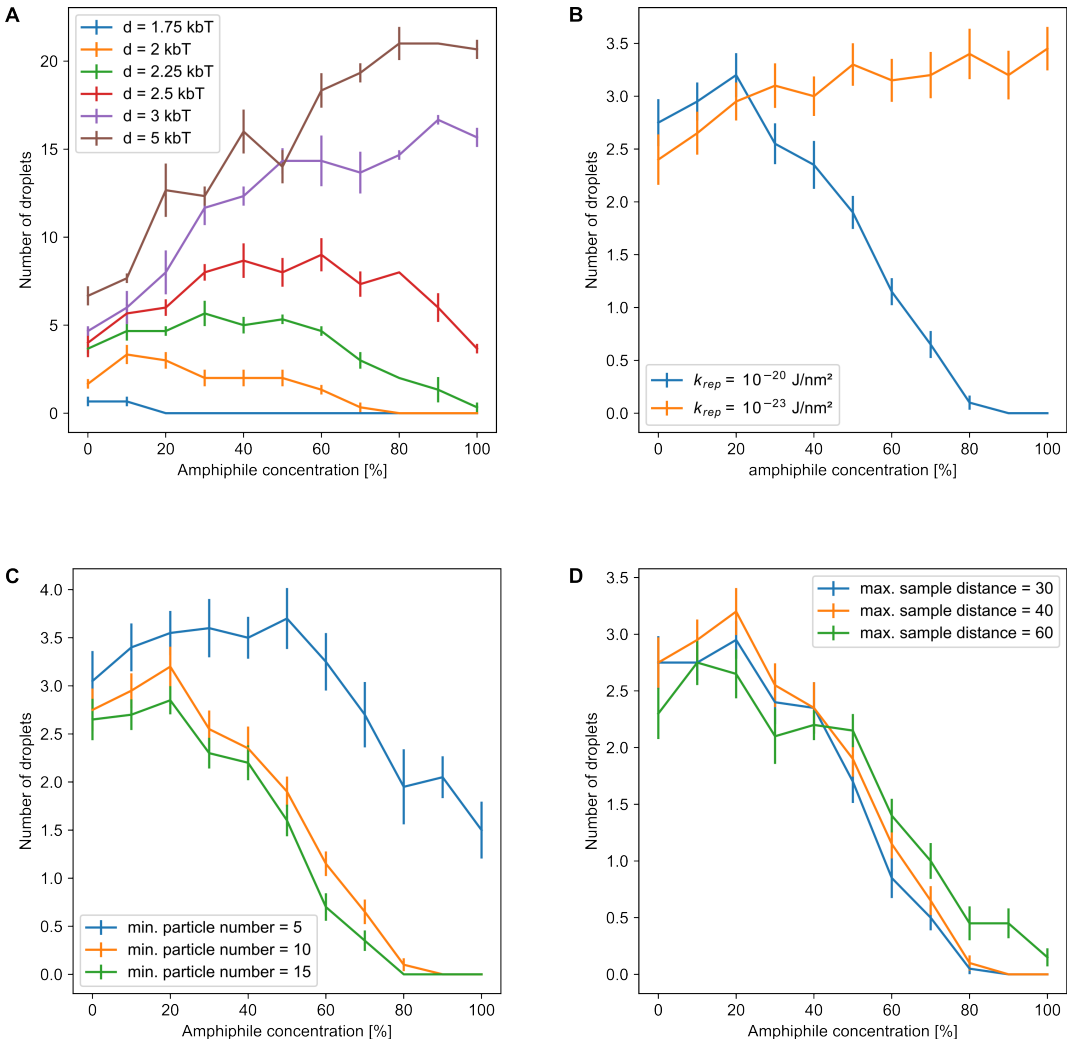

Fig. S3: **The number of detected droplets in the Langevin dynamics simulation for different simulation and evaluation parameters** A) To select the parameters of the Langevin simulation, we carried out out a simulated titration experiment that places 450 particles split between Y-motif and amphiphile in a spherical volume of radius 200 nm inside a simulation box of 1 μm edge length. We then examined the final number of droplets after 10^6 time steps. As the depth of the harmonic well potential introducing attraction between simulated Y-motifs increases, the peak number of detected droplets shifts towards higher amphiphile concentrations. We selected a value of $2k_bT$ as the resulting curve resembles the experimental observation. B) Keeping the depth of the well potential fixed at $2k_bT$ and decreasing the repulsion between ampihpihle and all other particles resulted in a continuous increase of droplet number, confirming that the ration of attractive to repulsive interactions determines the shape of the curve. C) Droplets were detected with the DB-scan algorithm using a minimum number of 10 particles for classification as cluster/droplet. Changing this value by 5 particles influences the shape of the curve but not the qualitative behaviour. D) In a similar fashion, the maximum distance between particles of one cluster can be varied from the 40 nm we settled on, without changing the qualitative behaviour of the curve. Panel A averages over 3 independent simulation runs, panels B, C, and D use 20 simulation runs with well potential depth of $2k_bT$.